Construction and Building Materials 435 (2024) 136794

Contents lists available at ScienceDirect

Construction and Building Materials

journal homepage: www.elsevier.com/locate/conbuildmat

Experimental and analytical analysis of the bond alteration of impregnated carbon fibre reinforcements embedded in alkali-activated concrete at elevated temperatures

Jitong Zhao [a], Cesare Signorini [a], Andrea Nobili [b], Marco Liebscher [a,*], Jan Kohout [c,d], Pavlína Hájková [c,d], Viktor Mechtcherine [a]

[a] Institute of Construction Materials, TU Dresden, Georg-Schumann-Str. 7, 01187 Dresden, Germany
[b] Department of Engineering "Enzo Ferrari", University of Modena and Reggio Emilia, 41125 Modena, Italy
[c] ORLEN UniCRE a.s., Revoluční 1521/84, 400 01 Ústí nad Labem, Czech Republic
[d] Department of Material Science, Faculty of Mechanical Engineering, Technical University of Liberec, Studentská 1402/2, 461 17 Liberec, Czech Republic

ARTICLE INFO

Keywords:
Carbon-fibre composite
Impregnation
Geopolymer
Reinforcement
Automation

ABSTRACT

The restricted operating temperature range of fibre-reinforced polymer (FRP) systems for upgrading and retrofitting reinforced concrete structures is among the key limiting factors of this technology. Indeed, an alternative reinforcing system, known as Mineral-impregnated Carbon-Fibre (MCF), has recently emerged to address this issue. This paper presents an experimental investigation of the performance of MCF systems embedded in fine-grained, Alkali-Activated Concrete (AAC), which have been pre-heated at 100 °C (or 200 °C) and then tested in pull-out at the target temperature. For the purpose of assessing the bond quality against thermal exposure, results are compared with the control group (ambient temperature 20 °C), as well as with an epoxy-impregnated commercial roving. In addition, specimens are characterised at the fibre-to-matrix interface by microscopy and by physical–chemical analytical techniques. Experimental data are fitted onto a one-dimensional stress-and-friction analytical model to determine the characteristic properties of the temperature-dependent bond–slip behaviour of MCFs. Findings suggest enhanced chemical compatibility and reinforcing capabilities at elevated temperature for MCFs, primarily ascribed to the impregnation quality and to the AAC capacity to withstand thermal strain.

1. Introduction

Fibre Reinforced polymer (FRP) composites are now widely adopted for civil engineering applications as high-performance externally bonded strengthening systems. Indeed, carbon fabric proves immune of the well-known corrosion issue typical of steel. In addition, FRPs offer superior versatility, ease of application, an outstanding strength-to-weight ratio and, overall, exceptional potential for optimisation at the design stage. Still, application of FRP composites suffer from serious concerns regarding their high temperature behaviour, specifically in terms of reduced strength, stiffness and bonding properties. The mechanical properties of FRPs are in fact adversely affected by temperature due to the intrinsic limitations of the polymeric phase, such as the glass transition temperature for thermosets, the melting point for thermoplastics and, ultimately, the decomposition temperature [1,2]. For this reason, more advanced composites have been developed in recent decades, replacing polymer matrices with mineral-bonded counterparts, such as cementitious binders. Composites combining technical fabrics made from synthetic fibres (e.g. carbon) with inorganic matrices are generally referred to as textile-reinforced concrete (TRC) and have been successfully employed for both structural strengthening and the production of new lightweight thin-walled structures.

However, when dealing with inorganic matrices, the presence of solid particles larger in diameter than the interstices between adjacent fibres prevents complete impregnation of the roving. This lack of impregnation by the embedding medium is often associated with the induction of telescopic failure and fabric slippage [3], which significantly impairs the full conversion of the mechanical potential of the reinforcing fibres. This issue has been extensively studied and technological approaches, such as bundle coating and impregnation during textile manufacturing, have become essential to bind the filaments together, ensure practical handling, provide an outer sheath to further protect

* Corresponding author.
E-mail address: marco.liebscher@tu-dresden.de (M. Liebscher).

https://doi.org/10.1016/j.conbuildmat.2024.136794
Received 28 February 2024; Received in revised form 28 April 2024; Accepted 24 May 2024
Available online 7 June 2024

the sleeve filaments from abrasion [4–6], and ultimately promote long-term performance [7]. The state of the art in this field consists of polymer impregnation strategies mainly involving epoxy resins [8,9], styrene-butadiene [10,11], polycarbonate-polyurethane [12], among others. Depending on the intended application, rigid impregnation phases such as epoxies generally yield the best overall performance of the TRC composite in terms of tensile strength, elongation and toughness [13], at the expense of textile flexibility, while a trade-off between mechanical response and textile flexibility is required for applications of curved TRC elements [12]. However, when polymer impregnation is used, thermal stability is compromised to some extent, as demonstrated by several studies [2,14], although the hydraulic matrix layer covering the roving has been shown to mitigate, or at least delay, this detrimental process [15,16]. Replacing polymer matrices with mineral impregnating agents appears to be a promising solution for improving the temperature resistance of textile-reinforced composites [1,4,17]. Some fibre coating techniques proposed in the literature involve the addition of hydrophilic particles, e.g., micro- and nanosized silica, which allow an improved, albeit partial, conversion of the textile properties [18]. Moving to inorganic bundle impregnation, good results have been obtained by cement-based Mineral impregnated Carbon Fibre (MCF) rovings, first developed by Schneider et al. [19] and then extended to poly(p-phenylen-2,6-benzobisoxazol) (PBO) fibres for structural retrofitting [20]. This innovative approach lends chemical affinity with the concrete matrix and it is able to uniformly penetrate the bundle well inside the rovings, thus preventing lack of adhesion while allowing significant cost reduction and technological flexibility in production and application [21,22]. Furthermore, recent findings have shown how tailored surface profiling of MCF enhances the shape stability and activates additional mechanical interlocking with the embedding matrix [23], with favourable implications for digital, automated robotic or additive manufacturing approaches [24]. While the proof of concept for cementitious impregnation has been largely established, challenges arise from the long hydration time of cement-based suspensions and from the large storage space required to allow for sufficient strength gain. These limitations restrict the availability of cost-effective manufacturing of MCF bars and/or textiles and their potential industrial upgrading. To improve the processability of MCF reinforcements, research has focused on alternative impregnating agents and curing processes to achieve MCF featuring sound and scalable performance and sustainability [25]. Among the existing mineral impregnation matrices, a promising approach is to replace cementitious materials with geopolymers (GP), which feature both a wider processing window for continuous impregnation and rapid setting with increased early strength through targeted low-temperature synthesis [26,27]. Nevertheless, understanding of the reinforcement capabilities of GP-MCF at temperatures in the range of 200 °C remains limited, although some contributions in the literature outline significant potential for GP-based composites, which have been investigated in a variety of applications, such as high-tech aerospace, automotive and engineering fields [28–33]. Some valuable attempts have been proposed for GP-based composites in the field of structural strengthening [34–37], with promising outcomes in terms of fire and thermal resistance [38,39].

To pave the way to the application of MCF systems to concrete structures, a systematic assessment of the parameters governing the interfacial interaction between GP-MCF rovings and the embedding mineral matrix is crucial. In fact, although GP impregnation is preferred in several respects over the use of cement, the main downside of this approach lies in the poor chemical affinity with standard cement-based matrices. Furthermore, high temperature exposure is expected to affect the force transfer pathways and the crack formation mechanisms in structural elements. To better elucidate such aspects, a simple mechanical model is resorted to, which describes both the elastic and the debonding progress. Kelly [40] may have been among the first authors to recognise the very different behaviour of ductile versus brittle matrix composite systems, and to relate this difference to the pull-out test. His approach, based on a constant stress distribution along the roving and focusing on gradual debonding, has been parallelled by many authors, such as Hutchinson and Jensen [41],Naaman et al. [42],Radi et al. [43],Sorzia et al. [44]. In contrast, Kerans and Parthasarathy [45] provide a critical review of previous models and in particular recognise the importance of accounting for the finite extent of the fibre anchorage until debonding gradually develops. It is precisely along these lines, which are also well illustrated by DiFrancia et al. [46], that the model in this paper considers a (depthwise) finite stress distribution that allows for progressive debonding, here assumed cohesive in nature for simplicity.

Table 1
Properties of Solidian GRID Q85/85-CCE-21 according to the manufacturer.

Property	Unit	Value
Fineness of the roving	tex	3200
Net cross-section of the roving	mm^2	1.81
Cross-sectional area of textile per unit width	mm^2/m	85
Mean tensile strength (ISO 10406-1)	MPa	3300
Modulus of elasticity (ISO 10406-1)	GPa	220
Impregnation type	–	epoxy

The present study aims to investigate the bond–slip behaviour of two different variants of GP-MCFs (namely, with and without surface profiling) when embedded in a fine-grained, alkali-activated concrete (AAC) matrix and exposed to three target temperatures, i.e. ambient (20 °C), 100 °C and 200 °C. To attain temperature uniformity within the specimens, the heating protocol consisted of a pre-heating phase of 2 to 4 h, respectively for 100 °C and 200 °C. Single-sided pull-out tests were then conducted at the target temperature. A commercial carbon roving impregnated with epoxy (E) resin serves as benchmark. The implications of both roving impregnation and surface profiling are studied.

2. Materials and methods

The experimental activity presented in this study consists of in-situ single-sided pull-out tests aimed at directly characterising the bond behaviour of impregnated rovings in an alkali-activated concrete (AAC) matrix. This section describes the raw materials that were considered, the specimen preparation and the test protocols that were followed.

2.1. Materials

The commercial, warp-knitted carbon grid (GRID Q85/85 – CCE – 21) supplied by Solidian GmbH (Albstadt, Germany) served as reference and is characterised by epoxy impregnation (see Fig. 1a). Each roving, either warp or weft, features a count of 3200 tex, an average tensile strength of 3300 MPa, and the glass transition temperature, T_g, for the epoxy impregnation is 115 °C. The main physical properties, as declared by the manufacturer [47], are given in Table 1.

For the production of mineral-impregnated carbon fibre (MCF) rovings, high modulus (HM) CF tow (SIGRAFIL® C T50-4.4/255-E100) was supplied by SGL Group, Wiesbaden, Germany, in spools containing 50k individual filaments with epoxy sizing. Table 2 reports the main physical properties, as reported by the supplier [48]. It should be noted that both carbon fibres exhibit similar properties, especially in terms of fineness, and this allows for a meaningful comparison [26].

The customised mix design and mixing procedure for impregnation followed previous studies by the authors [26,49] and was based on reactive metakaolin ($Al_2O_3 \cdot 2\,SiO_2$) (trade name Metamax) from BASF (Ludwigshafen am Rhein, Germany), potassium silicate activator Geosil® 14517 from Wöllner (Ludwigshafen am Rhein, Germany) and superplasticiser based on modified phosphonic acid salts Sapetin D27 from Wöllner (Ludwigshafen am Rhein, Germany) at a dosage of 4 wt% of the geopolymer. Mixing was performed using an IKA T50 digital ULTRA-TURRAX disperser for 7 min, followed by 10 min of vibration to eliminate trapped air bubbles.

Table 2
Properties of multifilament carbon fibre roving SIGRAFIL® C T50-4.4/255-E100 according to the manufacturer.

Property	Unit	Value
Number of filaments	–	50k
Fineness of the roving	tex	3450
Density	g/m^3	1.80
Filament diameter	µm	7.0
Filament tensile strength	MPa	4400
Filament modulus of elasticity	GPa	255

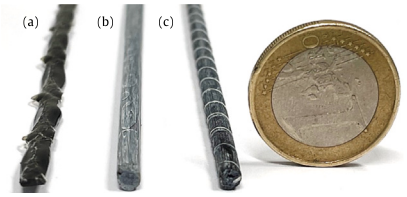

Fig. 1. Epoxy impregnated carbon roving ECF (a), and mineral impregnated carbon rovings without (b) and with (c) surface profiling, respectively S-MCF and W-MCF.

Table 3
Mix composition of the AAC matrix for the roving pull-out tests.

Constituent	Dosage [g/m^3]
Metakaolin	363
Ground-granulated blast-furnace slag (GGBS)	155
Fine sand 0–300 µm	264
Coarse sand 0–2 mm	759
Potassium silicate solution	519

2.2. Mineral impregnation of CF roving

Continuous impregnation of unidirectional rovings with the GP suspension was carried out in a pultrusion line driven by a fully digitalised control system as described by Liebscher et al. [50] and Zhao et al. [49].

The implementation of the MCF involved continuous drawing and winding of the roving onto a motor-driven hexagonal wheel. The roving passed through guide levels, a motorised kiss-coater and an impregnation bath consisting of a five-roller foulard system. To achieve a regular ellipsoidal cross-section, the impregnated roving was then formed by a plastic conical nozzle with an internal opening diameter of 4.1 mm. Some of the MCF rovings were further processed by applying an automatic helical winding to the semi-finished roving element at 6 mm intervals to achieve a corrugated surface (see Fig. 1c) [23]. To expedite the setting process, freshly impregnated rovings were thermally cured in an electric oven at 50 °C for 16 h. The appearance of the epoxy-impregnated control specimens (hereafter referred to as "ECF") as well as of MCF rovings, either with smooth ("S-MCF") or wound ("W-MCF") surfaces, is shown in Fig. 1.

2.3. Specimen manufacturing for pull-out tests

To investigate the interfacial bond properties of the three kinds of carbon multifilament rovings, a fine-grained, high-strength alkali-activated concrete (AAC) matrix was devised. Table 3 lists the composition of the mix, which consisted of metakaolin, ground granulated blast-furnace slag (GGBS), potassium silicate activator (Geosil® 14517), quartz fine sand (BCS 413 from Strobel, Germany) with a maximum particle size of 0.3 mm, and coarse sand (Ottendorf, Germany) with a maximum particle diameter of 2 mm.

To mitigate the adverse effects of aggregate fineness and high binder content in modern fine-grained concrete, the particle size distribution was carefully tailored to approximate an ideal target grading curve, i.e., the Fuller parabola [51]. The compressive and flexural strength values of the AAC matrix were tested on prisms (40 × 40 × 160 mm^3) at 20 °C, 100 °C and 200 °C according to EN 196-1 [52], while Young's modulus was measured at the same target temperature on prismatic specimens having the same dimensions, in compliance with EN 12390-13 [53]. Pull-out specimens consisted of two AAC blocks with dimensions of 90 × 80 × 80 mm^3 and 50 × 80 × 80 mm^3 (height × width × depth). The former served as an anchorage block and the latter as a test block. The roving was positioned at the centre of the two blocks, in fact connecting them, with a free length of 120 mm and an embedded length of 10 mm in the test block. An embedded length of 80 mm was chosen in the anchorage concrete block to ensure that the extraction would occur exclusively from the test block. Pull-out specimens were demoulded after 20 h, tightly wrapped in plastic bags and cured for further 27 days in a climatic chamber at 20 °C. The slump flow of the AAC matrix was 190 mm, determined using a Hägermann slump funnel in accordance with DIN EN 1015-3 [54], without application of strokes.

2.4. Testing methods

In order to characterise the bond–slip behaviour of the different rovings in the AAC matrix, one-sided pull-out tests were carried out using an Instron 8501 machine, equipped with a load cell Instron 2518-111. Most importantly, elevated temperature tests were directly conducted into a climatic chamber at a displacement rate of 1 mm/min at 100 °C and 200 °C and compared with reference samples, tested at ambient temperature (approximately 20 °C). This specific test protocol differs from preconditioning and allows the determination of bond properties at the target isotherm. Further information on the test setup can be found in Schneider et al. [55]. A minimum of five specimens were tested for each set. Prior to testing, the specimens were preheated in a Universal Furnace (UF1060 from Memmert GmbH + Co. KG) at a rate of 3 °C/min until the desired temperature was reached. Specimens were then held at the target temperature for 2 h and 4 h, to allow complete evaporation of physically bound water and part of chemically bound water, and to reach steady-state within the specimen. The time required to heat the entire embedded volume of the roving was determined using a type K thermocouple embedded in the centre of the concrete block.

The filament-matrix distribution, fracture surface, and failure behaviour of the rovings were investigated at the micro-scale using a Quanta 250 FEG environmental scanning electron microscope (FEI, Eindhoven, The Netherlands). A micro-computed tomography (μCT) scan CT-XPRESS (ProCon X-ray, Germany) with a high productivity 65 W X-ray tube and a high-resolution flat panel detector was performed to specifically investigate the roving-to-AAC matrix interface. Each scan lasted approximately 1 h with a sampling rate of 0.5 Hz and scanning conditions of 71 kV and 191 µA with 1441 projections. The scans were then iteratively reconstructed using X-AID software (MITOS, Germany), with 1470 × 1149 pixels for each slice.

Thermal expansion tests up to 200 °C were conducted using a dilatometer (Clasic CZ, type DIL 1500, Řevnice, Czech Republic) on both impregnation matrix and concrete matrix samples with dimensions of 20 × 20 × 160 mm^3. The measurements were performed at a heating rate of 3 °C/min for all the samples. Thermogravimetric analysis (TGA) was performed using a STA 409 DC thermal analyser (Netzsch, Germany). Samples were heated from 20 °C to 1000 °C at a rate of 10 °C/min in an O_2 flow of 60 mL/min. A Porotec PASCAL 140/440 porosimeter was employed to measure mercury intrusion porosity (MIP). The mercury surface tension was 0.48 N/m, the contact angle was 140°, and the test pressure ranged from 0 to 400.71 MPa. Prior to chemical characterisation, all samples were stored in liquid isopropanol for at least 24 h to arrest the hydration reaction, followed by drying in an Alpha 1–2 LDplus Christ vacuum desiccator for 7 days.

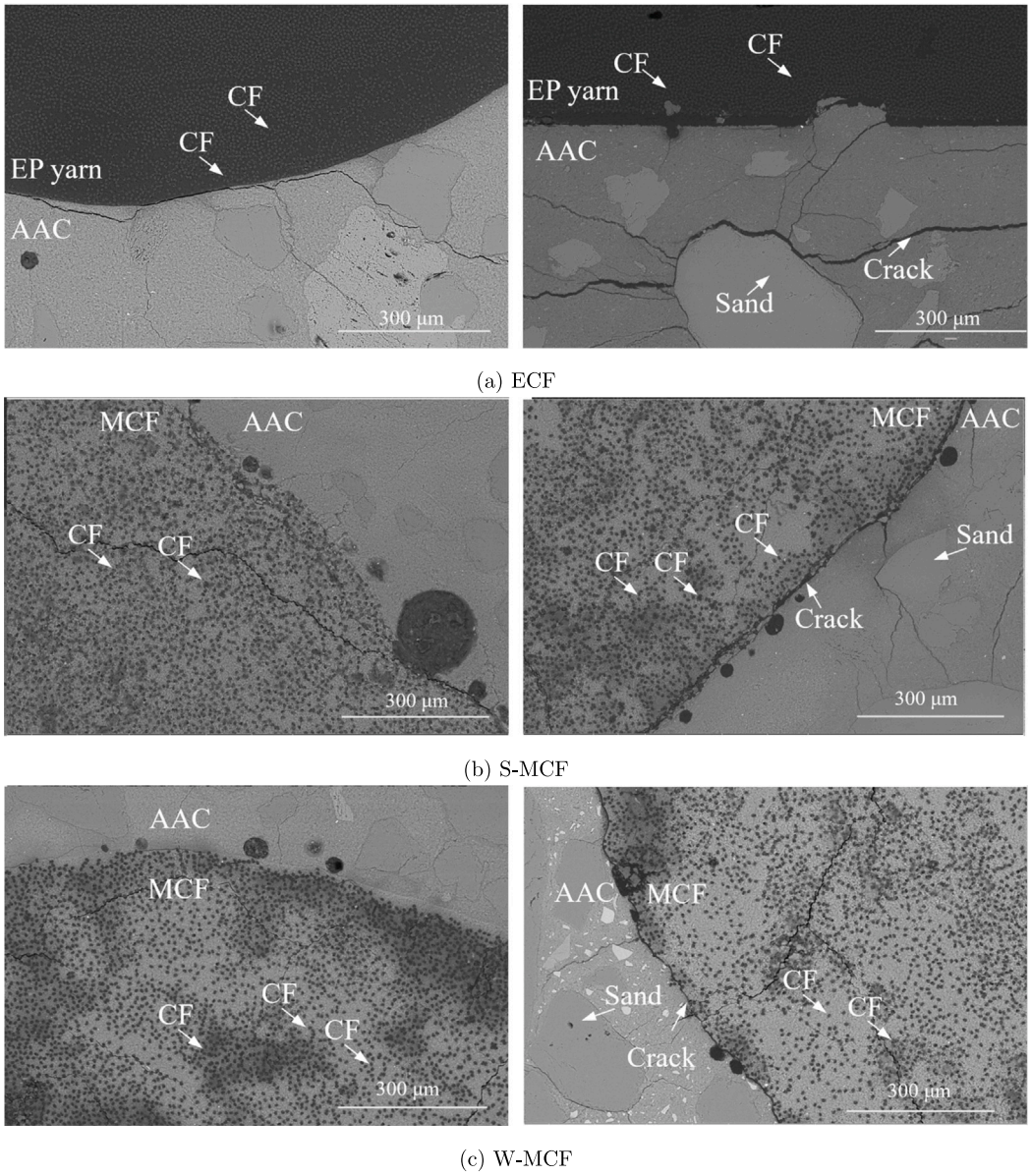

Fig. 2. ESEM images of the cross-sections at 20 °C (left) and 200 °C (right). The colour sequence of ESEM from dark to light represents the pristine CFs or epoxy resin, GP impregnation matrix, concrete binder materials, and concrete aggregate, respectively.

3. Results and discussion

3.1. Morphological and analytical characterisation of MCF and AAC matrix

The ESEM micrographs in Fig. 2 show the cross section of the rovings embedded in the AAC matrix. Comparisons are also presented between ambient temperature benchmarks (left inlets) and their counterparts tested at 200 °C (right inlets). As a general observation, the former micrographs confirm that the filament bundles were evenly penetrated by the impregnation matrix for both the ECF reference and MCF rovings. This evidence suggests that effective stress transfer between filaments has occurred during loading.

At room temperature, prior to the onset of debonding damage, the sleeve filaments are seamlessly surrounded by the AAC matrix with no visible boundaries, regardless of the impregnation medium. Specifically for the MCFs, the longitudinal sections were examined by μCT (see Fig. 3a), which show a continuous and intact interface. Such compact interfacial areas ensure effective confinement of the roving, fostering both the mechanical interlocking and the chemical bonding with the surrounding AAC matrix. In addition, the strong affinity between the GP impregnation and the embedding AAC here may promote the formation of a transitional interdiffusion boundary by assimilation. The debonding crack propagation observed in the MCF specimens was primarily within the impregnation matrix. This suggests a strong chemical affinity and moderate transverse stiffness provided by the GP impregnation matrix [23]. On the contrary, debonding in the ECF counterparts was mainly detected at the interface, suggesting that the mere frictional interlocking due to chemical incompatibility with the matrix was the underlying cause.

After preheating at 200 °C, the ECF rovings still display crack development in the interfacial zone (Fig. 2b), revealing the ongoing thermal degradation of the epoxy impregnation matrix. For MCFs exposed to 200 °C, premature cracking occurred within a few microns of the outer layer of sleeve filaments near the interface. Accordingly, the μCT slice of Fig. 3b showcases low density (i.e., black) areas that propagate axially between the MCF and AAC, highlighting the presence of voids and debonding cracks. This premature damage reduces the frictional interlock at the interface, and therefore the bond stress, and is attributed

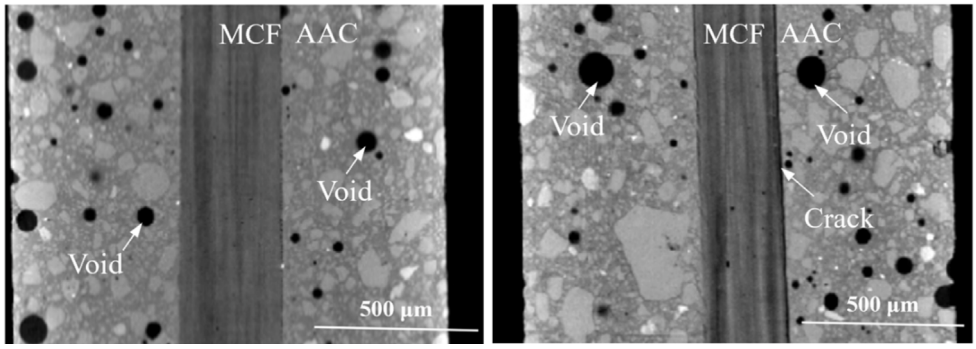

(a) 20 °C (b) 200 °C

Fig. 3. μCT slices of the pull-out specimens with the smooth MCF.

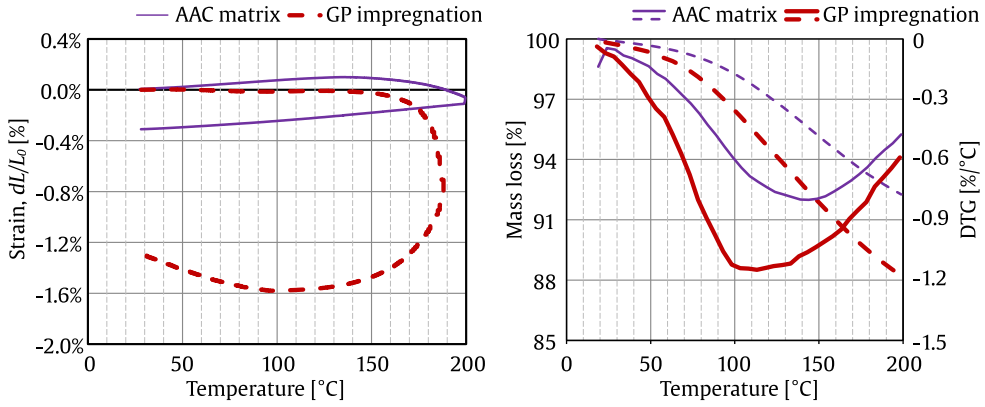

(a) (b)

Fig. 4. (a) Dilatometric curves and (b) TG/ DTG thermograms of the GP impregnating matrix and AAC matrix.

to thermal shrinkage during the preheating phase in the interface zone. Inevitable capillary cracks in the AAC matrix and GP impregnation are also visible at 20 °C due to autogenous and drying shrinkage, with their size and shape increasing as the temperature rises from 20 °C to 200 °C [56]. The implications of thermal shrinkage are currently the main challenge for GP mineral impregnation technology, especially when compared with cementitious impregnation, which undergoes thermal expansion upon heating [57]. The thermal shrinkage of the AAC matrix reduces the compaction pressure on the fibre reinforcement [51,55]. The phenomenon of cracking at the edge of the aggregate is presumably caused by the mismatch of volumetric changes between the sand aggregates and the alkali-activated gels [58], and is shown in Fig. 2b and d.

The thermal expansion curves for the AAC matrix and the GP impregnating suspension are shown in the dilatometric diagrams in Fig. 4a. For the GP impregnating agent, a slight deformation was recorded up to 150 °C, followed by significant shrinkage up to around 0.6 % at higher temperatures. This extent of shrinkage can be attributed to thermal dehydration, i.e., the evaporation of physically and chemically bound water, which typically occurs in this temperature range [59] and is evidenced by the thermogravimetric curve in Fig. 4b. As a result, the formation of voids or cracks within the MCF itself and interfacial debonding of the reinforcement is unavoidable. Conversely, the AAC matrix expanded up to 150 °C due to thermal expansion of the inert quartz sand. Thereafter, considerable shrinkage occurred, dominated mainly by thermal decomposition of the binder materials, which outweighed the expansion of the sand. As in the case of GP impregnation, the shrinkage of the AAC matrix after 150 °C is traced back to a pronounced dehydration of physically and chemically bound water [59,60], in good agreement with the observations made

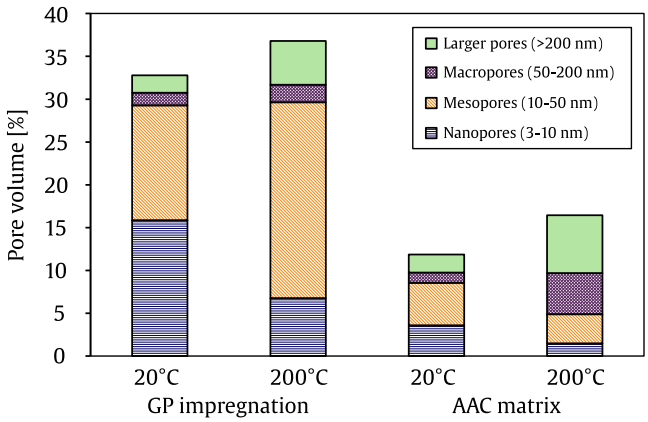

Fig. 5. Pore volume distributions obtained in MIP, as a function of the test temperature.

by TGA (see Fig. 4b). Interestingly, the peaks at 118 °C and 144 °C in the DTG for the GP impregnation suspension and AAC matrix, respectively, appeared earlier than the corresponding inflection points in the dilatometric curves. This minor difference can be explained by the different sample sizes and corresponding surfaces. Due to the higher water content in the GP suspension design, more pronounced dimensional deformation is recorded for the impregnating suspension, implying a dominant role in controlling the thermomechanical failure of the overall composite system.

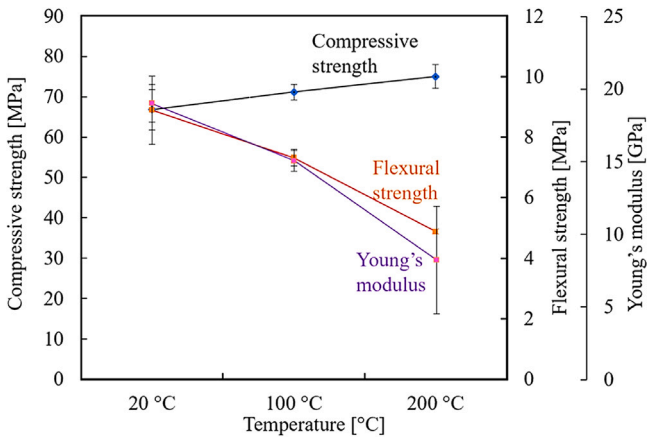

Fig. 6. Mechanical properties of the AAC matrix at elevated temperatures.

The bar charts in Fig. 5 provide an overview of the porosity of the two alkali-activated materials investigated here as the GP impregnating agent and the AAC matrix. The pore volume distribution of the specimens exposed at different temperatures can be classified into nanopores (3–10 nm), mesopores (10–50 nm), macropores (50–200 nm), and voids > 200nm, following the methodology of the previous study by Zhao et al. [49]. As the exposure temperature increases, both the impregnation suspension and AAC matrix show a substantial increase in their total porosity, mesopores, macropores and voids > 200nm as a result of the loss of water, while the proportion of nanopores is reduced. In fact, nanopores are closely interrelated with the intrinsic microstructure formation of the reaction products, whereas mesopores, macropores and those larger than 200 nm are indicative of dehydration and microstructural damage [61]. The increase in specific pore volume across all size ranges results in a loosely bound microstructure, ultimately leading to premature failure under load [62] and lower flexural strength and Young's modulus of AAC at higher temperatures.

As indicated in Fig. 6, the AAC investigated here exhibited a considerable reduction in flexural strength and Young's modulus when exposed to elevated temperatures up to 200 °C. The detrimental effect on the mechanical response is mainly ascribed to the dehydration of the binders, resulting in irreversible thermal shrinkage [63], as envisaged by TGA and dilatometric tests. Conversely, a modest increase in the compressive strength was observed, potentially related to the acceleration of the chemical reaction of the blended binders [64].

3.2. Pull-out behaviour of the MCF rovings

Pull-out tests under ambient and elevated temperature conditions disclosed the typical pull-out failure, with no visible concrete splitting or bar rupture. A detailed representation of the debonding process is shown in Fig. 7 in terms of shear force vs displacement curves for ECF, S-MCF and W-MCF, reported in different colours according to temperature exposure, i.e., blue for 20 °C, orange for 100 °C and red for 200 °C. The displacement is intended as the slip between the roving and the surrounding matrix block.

Distinct trends in the pull-out curve profiles clearly distinguish the epoxy-impregnated rovings from the MCF rovings. The former followed a three-branched curve, which is typical for FRP, as described in the work by Lorenz et al. [65]. Indeed, as the ECF roving progressively debonds from the surrounding inorganic matrix, the load increases until it reaches the peak debonding stress (τ_d) at the corresponding slip and fails at the fibre-matrix boundary due to poor chemical bond [51]. During the testing phase, both the force and the relative displacement (slip) from the machine were recorded up to a roving slip of 5 mm. The peak value is considered to be the interfacial bond strength (τ_{max}) and quantifies the combination of physical and chemical bond quality established at the interface, uniformly averaged over the entire embedded length. The interfacial bond strength was calculated by dividing the peak force by the lateral area of the embedded roving, which was assumed to have an approximately elliptical cross-section. The height and width of the roving were measured for each specimen [22,51]. The bond modulus (BM) was assessed as a secant modulus recorded between 20 % and 70 % of the maximum shear stress in the ascending branch of the stress–displacement curve. Owing to the high stiffness of CFs, the axial deformation of the free roving during the initial phase is minimal and can be neglected without impairing the accuracy of the measurement. The crack-bridging capacity of MCF rovings in AAC was estimated by taking into account the pull-out stress at the slip values of 0.5mm and 1.0mm ($\tau_{0.5}$ and $\tau_{1.0}$, respectively) in the post-peak phase for small crack widths, i.e., its serviceability, and large component deformations, respectively [66]. During the debonding stage, the slope of the ascending branch gradually declines as a result of the progressing detachment of the roving from the deeper cross sections. After attaining the peak bond stress, slip-softening occurred, showing the gradual decay of the frictional force in the extraction phase, with slight rises caused by additional frictional and bearing stresses due to the pronounced mechanical interlocking of the wrap-knit texture on the roving surface and the high stiffness of epoxy impregnation. Compared to epoxy-based rovings, the smooth MCFs show comparable bond strength, but higher bond modulus (BM) and slightly lower post-crack stress retain ($\tau_{0.5}$ and $\tau_{1.0}$). The curve profile of S-MCF is characterised by a more rapidly increasing branch during the initial loading stage until the peak debonding force is reached at a smaller displacement, signifying a higher shear modulus. This is accompanied by a subsequent steep drop, reflecting the failure of the adhesive bond in the outer filament layer. It is noteworthy that the initial almost linear elastic rise turns into a non-linear path with a decreasing slope before reaching the peak, indicating a gradual delamination process from the matrix. As described in earlier study [23], the crack propagation has been observed primarily within the impregnation matrix for the failed MCF specimens, suggesting strong chemical affinity and moderate transverse stiffness provided by the GP impregnation matrix. The pull-out process of the smooth MCF was associated with a mild softening branch or even a stress plateau, primarily influenced by friction and substantial shape interlocking. The additional tailored surface profiling of the wound MCF resulted in a 46 % increase in debonding stress, τ_d. In fact, as a bonded, deformed MCF bar is subjected to increasing axial tensile loads, the chemical adhesion between the MCF and the matrix gradually decreases. At the same time, additional surface deformations induce oblique contact forces directed towards the surrounding matrix. The stress on the surface of MCFs resulting from the force component in the direction of the bar can be interpreted as the bond stress between the MCF and the concrete matrix. The resistance in the post-cracked phase, which is ruled by friction, clearly benefited from the mechanical surface profiling. After attaining the first peak value, the declining trend of the bond stiffness is less pronounced than that of the smooth counterpart, while the subsequent pull-out phase is recognised by a non-linear ascending progression up to the maximum pull-out load. For instance, $\tau_{1.0}$ yields gains of 47 % and 20 % at 20 °C and 200 °C, respectively, over the smooth counterparts, respectively. A shift in the dominant mechanism of bond failure is argued, involving shearing of the surface indentations at the interface induced by the profiling and peeling of the AAC matrix. This process is dependent on the interplay of factors such as the relative shear strength between the fibres and the GP impregnation matrix, and the shear strength of the AAC matrix.

The bar charts in Fig. 8 present a comprehensive summary of the key results of τ_d, τ_{max}, $\tau_{0.5}$, $\tau_{1.0}$, $W_{0.5}$ and the Temperature Influence Factor (TIF). The TIF is calculated as the ratio of the values of τ_{max} at elevated temperatures to their counterparts at ambient temperature and is a direct indicator of performance degradation.

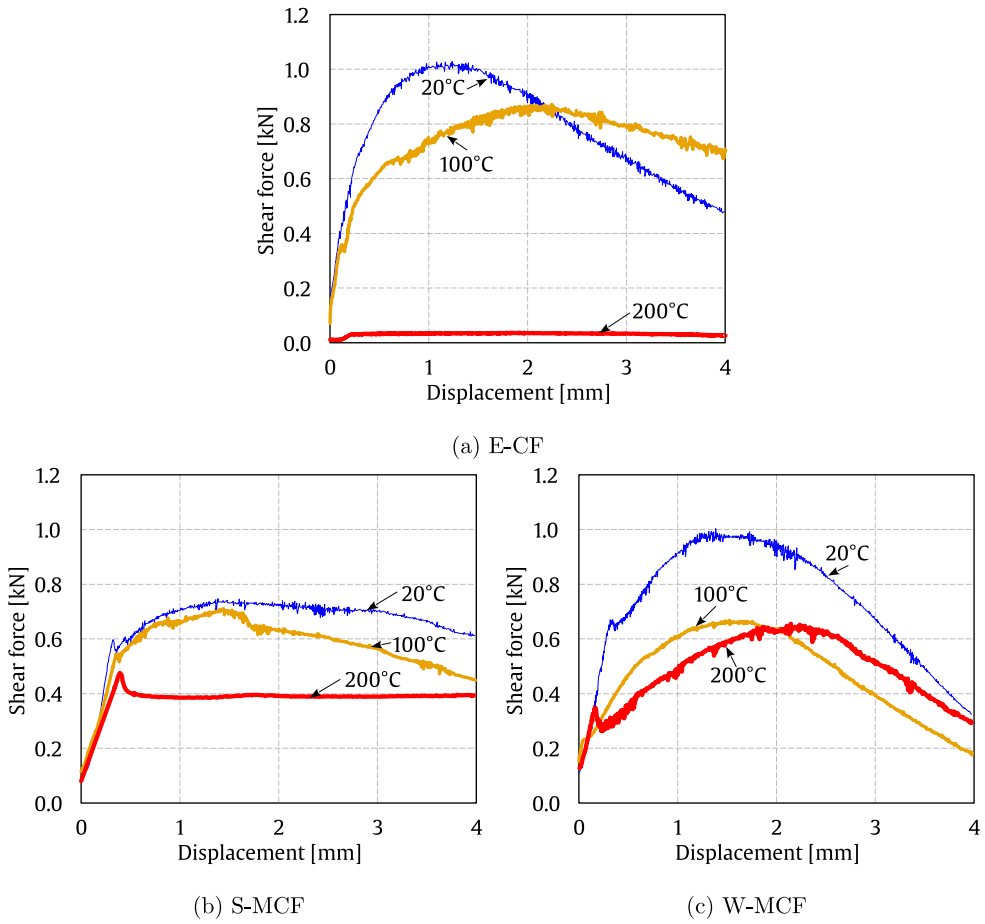

Fig. 7. Representative pull-out force–displacement curves obtained at different temperatures, i.e., 20 °C (blue), 100 °C (orange) and 200 °C (red). (For interpretation of the references to colour in this figure legend, the reader is referred to the web version of this article.)

With increasing exposure temperature, the TIF values and other parameters, including τ_d, τ_{max}, BM, $\tau_{0.5}$, and $\tau_{1.0}$ in the pull-out phase, consistently exhibit a gradual decline for both the ECF and MCF rovings, while maintaining similar debonding behaviour to the cases at 20 °C. Exposure of the ECF rovings to 100 °C suffers a moderate 25 % reduction in bond strength, which is limited by the residual shape interlocking. On the other hand, further heating to 200 °C resulted in an almost complete loss of bond strength, in line with previous findings for FRPs [67]. At this extent of thermal exposure, well above the glass transition temperature of conventional epoxies, a marked reduction in frictional bonding and mechanical interlock during the pull-out process is unavoidable due to softening or melting of the epoxy resin [68]. On the contrary, the superior durability of MCFs was demonstrated. Indeed, while at 100 °C both MCFs showed a slightly lower TIF than their epoxy counterparts, even at 200 °C they could still retain more than half of the corresponding bond strength at ambient temperature, i.e., 57 % and 50 % for S- and W-MCF, respectively. Similar trends were also observed for the $\tau_{0.5}$, $\tau_{1.0}$, during the post-peak phase and BM values for the three roving variants. The overall debonding failure of the MCF links to the multifaceted nature of the transverse shrinkage of the impregnation matrix and AAC and the axial mismatch between the carbon roving and the concrete substrate, as supported by dilatometry measurements (see Fig. 4). Compared to the softening of the polymer material, thermal strains have a lesser effect on the strength and stiffness of the AAC matrix and the MCF. The derived surface profiling on MCF results in lower TIF values at either 100 °C or at 200 °C compared to smooth counterparts, despite higher absolute values of the bond strength. The additional interlock stemming from the surface corrugation is expected to be weakened to some extent by the thermal shrinkage of the binders.

4. Mechanical modelling

A one-dimensional mechanical model is employed to assess the impregnation capabilities to promote adhesion to the matrix and elevated temperature stability. The model embodies the simple idea of simulating the rovings as a cylindrical rod of radius r under axial tension. Consistent with the test setup, the rod is partially embedded in the matrix (embedded length, t) and partially protruding (free length, l_0), as illustrated in Fig. 9.

The rod interacts with the matrix through a shear stress distribution across the mantle. Following Kerans and Parthasarathy [45] and DiFrancia et al. [46], it is assumed that the shear stress decays exponentially along the axial direction, x, pointing inside the specimen, namely

$$\tau(x) = \tau_0 \exp(-\chi x), \quad 0 < x < t. \tag{1}$$

In Eq. (1), the rate of decay $\chi > 0$ is directly connected to the *extinction length* L_e, also named the *elastic effective bond length*, i.e., the distance beyond which the roving feels a negligible pull-out force, e.g., $\exp(-\chi L_e) = 1\%$, see [46] and references therein. As the external pull-out force F increases, the shear stress function still retains the form (1), with the understanding that the peak shear stress $\tau_0 = \tau_0(F)$ is monotonically increasing with the applied force F. As a result, the decay rate (and likewise the extinction length) is assumed to be *independent* of the applied force. During this stage, the force–displacement curve is linear and its slope, E_t, reflects the axial stiffness in the rod. This behaviour should be contrasted with the cohesive material law (CML) pure-Mode-II models of fracture, which appear in the literature (e.g., [69,70]), and stipulate a CML in terms of tau-slip, the latter being

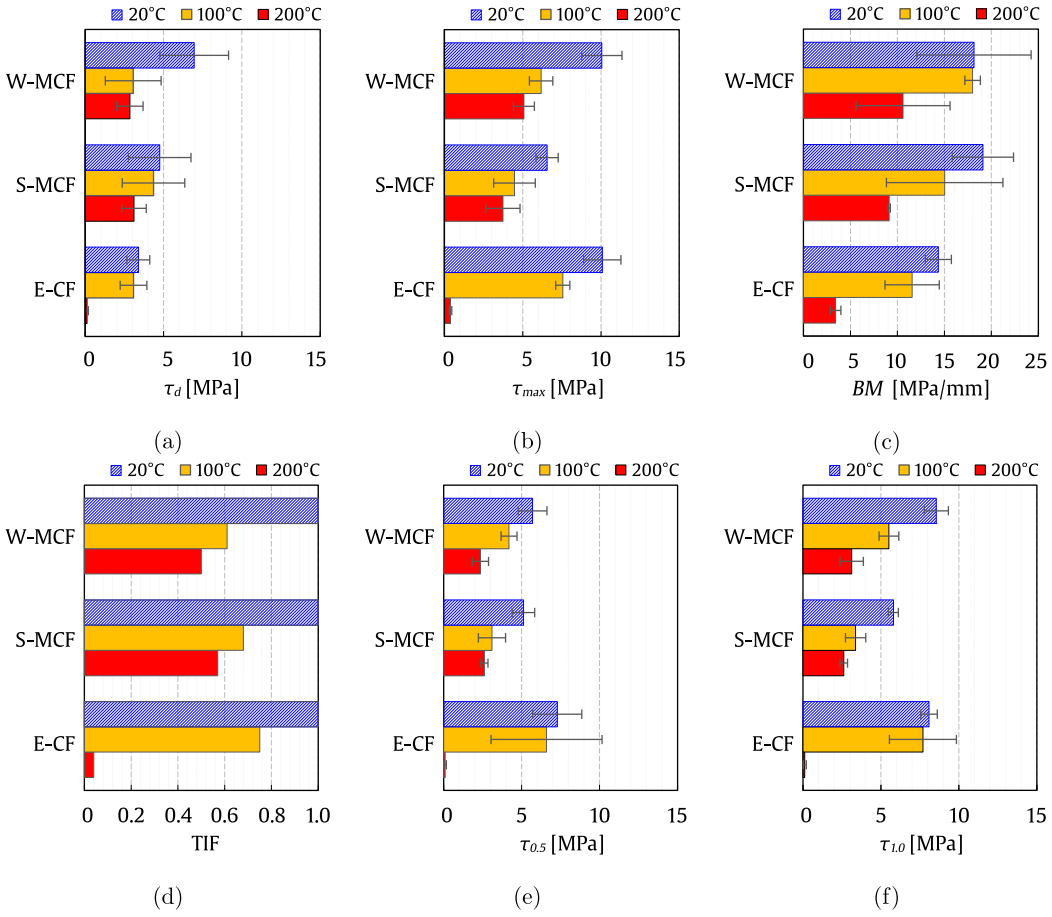

Fig. 8. Average mechanical parameters obtained by experimental tests as a function of the temperature exposure for each impregnated roving.

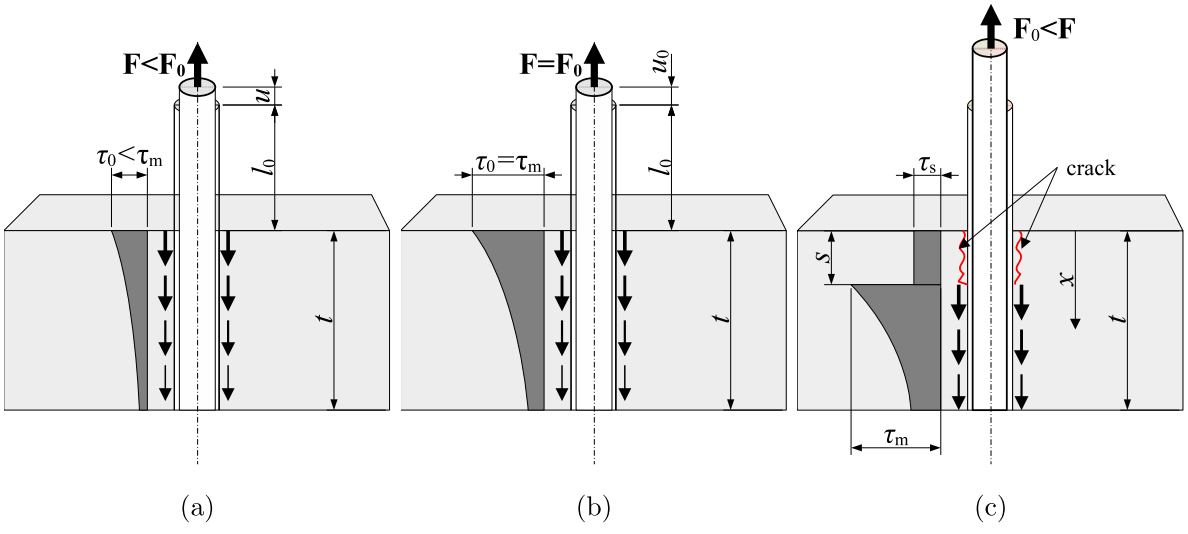

Fig. 9. Pull-out of a fibre embedded in a matrix with embedded length t. Initially, the applied force $F < F_0$ is transmitted to the matrix through the shearing force distribution (a), at $F = F_0$ the maximum shear force that may be transmitted to the matrix, τ_m, is reached (b), later debonding develops over the length $s < t$ and frictional shear $\tau_s < \tau_m$ arises: this lends the hardening part of the strength curve.

intended as "the relative displacement at the debonding interface". In such models, in the absence of slip, the shear stress is constant. Instead, we follow the concept by DiFrancia et al. [46], according to which it is "the load versus crack-length relationship which must be implemented", as opposed to "the load versus displacement relationship". In the absence of catastrophic failure, a crack may develop within the material, with a length that may not be equal to the fibre's slip. When the threshold force $F = F_0$, which corresponds to the threshold stress $\tau_0 = \tau_m$, is reached, interface damage develops and longitudinal cracking occurs starting from the matrix surface along the rod mantle. Enforcing the boundary condition demanding that the normal force in the roving, $N(x)$, is zero at the bottom surface of the matrix, i.e., $N(t) = 0$, yields the threshold shear stress τ_m as a function of the decay rate χ and of the pull-out force F_0

$$\tau_m = F_0 \frac{\chi e^{\chi t}}{2\pi r (e^{\chi t} - 1)}.$$

As a result of longitudinal crack formation, the exponentially decaying shear stress distribution moves deeper into the matrix, at depth s, and it is replaced by a (possibly frictional) constant cohesive shear stress $\tau_s = \eta^{-1}\tau_m$, where $\eta > 1$, namely

$$\tau(x) = \begin{cases} \tau_s, & x < s, \\ \eta\tau_s \exp(-\chi x), & s \le x \le t \end{cases} \tag{2}$$

This second stage clearly features a non-linear force–displacement response for $F > F_0$ and $u > u_0$, which is of most interest in assessing the mean interfacial strength. In fact, it is at this stage that interfacial damage takes place and hardening occurs in the force–displacement curve. The mean interfacial strength indeed determines the extent of this hardening branch, while the maximum transmitted shear stress propagates steadily downwards along the roving. This distinctive behaviour is associated with progressive, as opposed to catastrophic, failure at the interface and can only occur inasmuch as $\eta > 1$. The significance of this hardening branch lies in the ductility and resistance that it provides.

At the end of this hardening branch, the maximum force F_1, corresponding to the displacement u_1, is reached when the exponentially decaying stress at the bottom surface matches the cohesive shear stress in the crack, i.e., $\tau(t) = \tau_s$. This condition yields the maximum crack length $s_1 = t - \chi^{-1}\ln\eta$ in the matrix. Indeed, beyond this point, the cracking process becomes catastrophic, although some residual frictional resistance may be retained. From a mechanical viewpoint, this outcome is due to the fact that the newly generated cohesive frictional stress, τ_s, is unable to counterbalance the diminishing contribution offered by the exponentially decaying stress block, which has shifted deeper in the material and it has consequently become shorter, due to the finite embedment length. The final stage, which occurs for $F < F_1$ and $u > u_1$ and corresponds to the softening branch of the force–displacement curve, is mainly indicative of the frictional effects of pulling the roving out of the cracked matrix. Such a response is inherent to a weak interface and often occurs in textile reinforced systems in the absence of roving impregnation [71,72].

Following the approach described by Signorini et al. [20], the model is conveniently reformulated in terms of dimensionless parameters for the axial coordinate ($\zeta = x/t$) and the decay rate ($\kappa = \chi t$), which yield the dimensionless strength curve in the hardening regime F/F_0

$$F/F_0 = f(\zeta) = \frac{e^{\kappa}(\zeta\kappa + \eta) - \eta e^{\zeta\kappa}}{\eta(e^{\kappa} - 1)}, \tag{3}$$

and the area under the corresponding curve

$$A_1 = \int_0^{\zeta_m} F/F_0 \mathrm{d}\zeta = \frac{e^{\kappa}\left(\zeta_m^2\kappa^2 + 2\eta\zeta_m\kappa - 2\right) + 2\eta}{2\eta(e^{\kappa} - 1)\zeta_m\kappa}. \tag{4}$$

Indeed, Eq. (3) approximates the additional force demanded beyond the linear regime in the slip-hardening phase (with $\zeta \in [\zeta_0, \zeta_1]$), while Eq. (4) defines the dimensionless area under the strength curve up to the maximum point $[\zeta_m, F_1/F_0]$, where $\zeta_m = \zeta_1$ and $F_1/F_0 = f(\zeta_m)$. It is noteworthy that such quantities are defined in terms of two parameters only, namely η and κ, which, in fact, may be determined by curve fitting.

4.1. Data filtering and parameter calibration

The experimental data sets were first filtered by taking the 10-neighbour mean at each data point, to get away with the usual noise associated with the experimental procedure which may blur the underlying trend. The linear regime, which occurs up to force F_0 and displacement u_0, is then considered and the corresponding best fit line is drawn, which provides the stiffness E_t, similar to the (tangent) Young's modulus, as well as the precise amount of shift which is required to consistently align data curves across different specimens. This shift is set so that zero intercept with the load axis is obtained at zero displacement, i.e., curves start from the origin.

Once the linear regime is identified, the debonding process is described according to the proposed model and the experimental curve is fitted against the expected behaviour (3). The mechanical parameters η and κ are then obtained, bearing in mind the following constraints:

1. $\eta < \exp\kappa$, $\kappa > 0$;
2. the area under the curve in the slip-hardening regime obtained from the data set corresponds to (4);
3. the bond quality affects κ and η simultaneously, therefore we demand $\eta > 1 + \kappa/10$.

From a physical standpoint, the third restriction expresses the expectation that better adhesion with the matrix entails greater maximum shear stress, τ_m, and shorter extinction length, χ^{-1}. Numerically, this constraint prevents the fitting algorithm from hitting the boundaries of the optimisation region for one parameter and then seeking the optimum value for the other. The relationship between adhesion quality and extinction length is also supported by the results on PBO fibres in Signorini et al. [20], which indeed suggest that the interfacial bond strength affects the decay rate of the shear stress field.

In the following, the results of data fitting are illustrated for each roving type, namely epoxy (ECF), smooth (S-MCF) and wound (W-MCF) mineral impregnation. Emphasis is placed on the calibration of the mechanical parameters, η and κ, which characterise the interfacial bond, at both ambient temperature and 100 °C exposure. In fact, the data set for 200 °C exposure, that is associated with a shift in the failure mode due to interface degradation, exhibit too much scattering to allow for meaningful data fitting, despite robust filtering. Consequently, the corresponding modelling parameters are associated with large CoV and therefore are not reported in this study. A wrap-up discussion of all fitted parameters, pertaining to both the linear and the slip-hardening phase, is given in Section 4.2.

4.1.1. ECF datasets

Fig. 10a shows the linear fit inside the filtered experimental curve for all specimens, while Fig. 10b zooms in the linear regime up to $F_0 = 0.5$ kN. In particular, the quality of the linear approximation appears to be satisfactory, although the stiffness E_t was found to vary significantly among different specimens.

The fitted parameters η and κ are gathered in Table 4 for each specimen together with the standard error, the mean across and the coefficient of variation (CoV) for the mean. Specimen 3 in the ECF-20 °C group behaves strongly out of trend and it is therefore excluded from the mean.

Data pertaining to specimens exposed at 100 °C appear consistent, although data scattering increases, as it may be expected, owing to the degradation of the impregnation and of the interface. Quantitatively, the analysis of the fitting residuals shows that the deviation from the actual data set lies below 5% throughout the entire slip-hardening regime (an example is shown in Fig. B.14 in the Appendix).

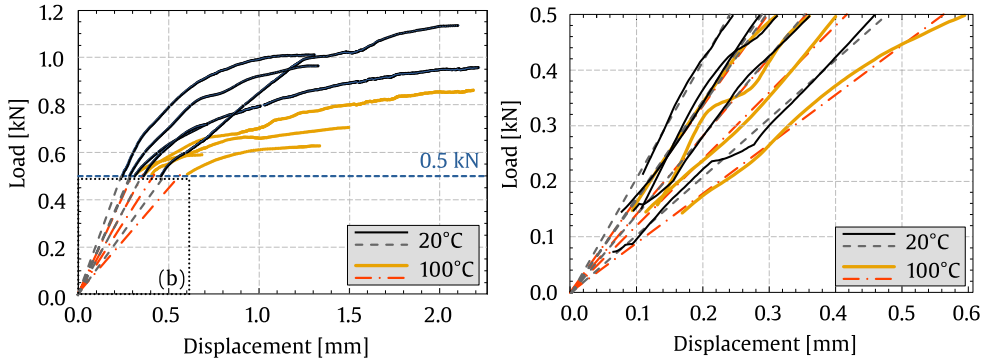

(a) Slip-hardening stage (b) Linear stage fitting

Fig. 10. Filtered data sets for ECF specimens (solid curves) used for model fitting in the linear and post-linear (slip-hardening) regimes. The linear fit (either dash-dotted or dashed lines) is plotted over the filtered data sets in inlet (b). The linear regime is conventionally set up to $F_0 = 0.5\,\text{kN}$.

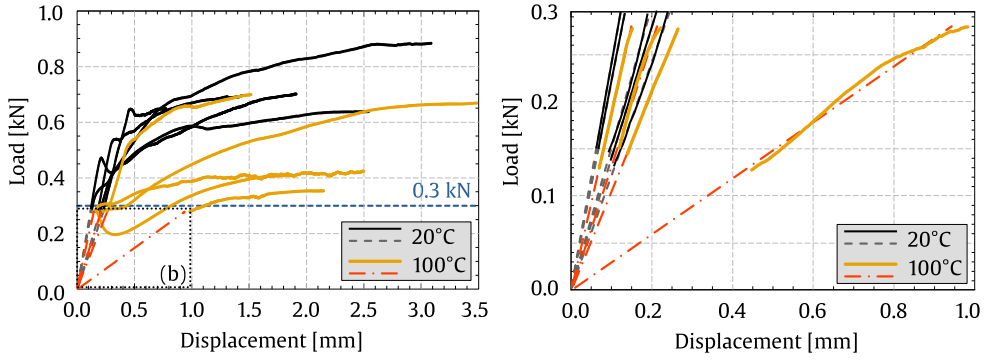

(a) Slip-hardening stage fitting (b) Linear stage fitting

Fig. 11. Filtered data sets for S-MCF specimens (solid curves) used for model fitting in the linear and post-linear (slip-hardening) regimes. The linear fit (either dash-dotted or dashed lines) is plotted over the filtered data sets in inlet (b). The linear regime is conventionally set up to $F_0 = 0.3\,\text{kN}$.

4.1.2. S-MCF datasets

Similarly to the dealing of ECF, the filtered experimental data for smooth mineral-impregnated fibres (S-MCF) and the corresponding best-fitting lines are displayed in Fig. 11, for the slip-hardening and the linear regimes. Again, the inlet zooms on the linear approximation, this time up to $F_0 = 0.3\,\text{kN}$.

It is clear that two specimens exposed at 100 °C are obviously off-trend, i.e. one is exceptionally tough and the other behaves non-monotonically after the linear regime (although, the linear trend for this specimen matches perfectly that of other specimens). The interpolation parameters of the slip-hardening branch, which are an indication of the interphase bonding capability, are collected in Table 5 where, in particular, the mean for η and κ is obtained discarding the two specimens that exhibit a clear off-trend response.

4.1.3. W-MCF datasets

As with the previous data sets, Fig. 12 illustrates the filtered strength curves alongside the linear approximation that is zoomed in the inlet; the linear regime is set up to $F_0 = 0.5\,\text{kN}$ and $F_0 = 0.45\,\text{kN}$ respectively for ambient temperature 20 °C and 100 °C exposure. Specimens exposed at 100 °C exhibit a wide range of stiffness, which is also reflected in the coefficient of variation for E_t.

The interpolation parameters for the slip-hardening branch of W-MCF are summarised in Table 6. Unexpectedly, the table shows that the mean value for η at 100 °C is higher than that obtained at ambient temperature, although the statistical significance of this increment is doubtful in light of the large associated CoV (73 %).

4.2. Discussion

Fitting parameters for both the linear and the slip-hardening regimes are gathered in Fig. 13, where, for the latter, the peak load, F_1, and the maximum corresponding displacement, u_1, are also shown, together with the area under the hardening curve, A_1.

Looking at the main mechanical indices emerging from the tests conducted at ambient temperature (20 °C), it appears that, contrarily to expectation, S-MCF generally exceeds ECF. The sole notable exception is constituted by stiffness, E_t, that increases moving from ECF to S-MCF and finally to W-MCF, the last showing a 50 % increase over the first, most likely due to improved surface roughness due to winding. Interestingly, this stiffness increase occurs while the CoV remains stable or even decreases, which fact suggests that this stiffness gain is statistically significant. Of course, given that the limiting force F_0 is similar for all the groups, this stiffness increase comes at the expense of elongation, and indeed u_0 drops by 41 % for W-MCF with respect to the epoxy-impregnated ECF. However, this pattern is not replicated in the slip-hardening regime, as the peak force F_1 for W-MCF remains slightly higher than that of ECF, with an even greater elongation u_1.

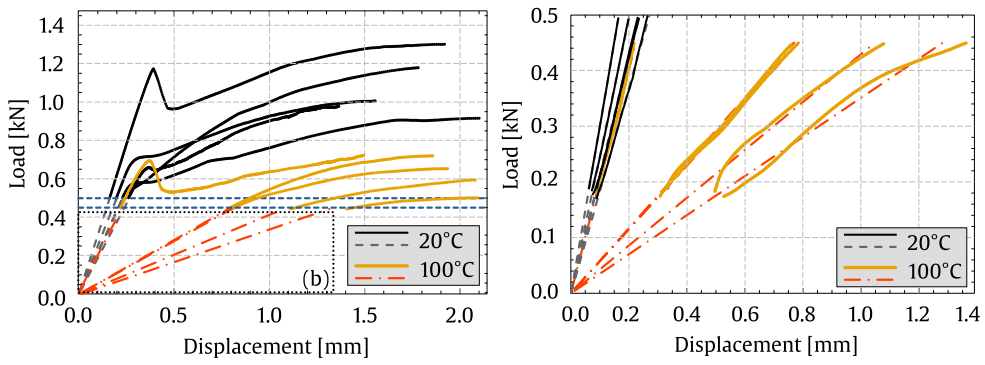

(a) Slip-hardening stage fitting (b) Linear stage fitting

Fig. 12. Filtered data sets for W-MCF specimens (solid curves) used for model fitting in the linear and post-linear (slip-hardening) regimes. The linear fit (either dash-dotted or dashed lines) is plotted over the filtered data sets in inlet (b). The linear regime is conventionally set up to $F_0 = 0.45\,\text{kN}$ and $F_0 = 0.5\,\text{kN}$ for 20 °C and 100 °C, respectively.

Table 4
Fitting parameters η and κ for the load ratio F/F_0 in the hardening regime, for each specimen in the ECF group, exposed at ambient temperature 20 °C and at 100 °C.

E-CF	20 °C						100 °C				
	sp1	sp2	(sp3)	sp4	sp5	Mean[a]	sp1	sp2	sp3	sp4	Mean
η	1.24	1.24	15.91	1.26	1.20	**1.24**	1.18	1.06	1.09	1.51	**1.21**
std.err.	0.26	0.21	3.94	0.10	0.13	CoV 2%	0.23	0.30	0.20	0.21	CoV 20%
κ	2.38	2.44	11.51	2.62	2.04	**2.37**	1.81	0.62	0.91	1.04	**1.10**
std.err.	0.64	0.52	2.27	0.26	0.30	CoV 10%	0.52	0.57	0.39	0.23	CoV 46%

[a] Excluding sp3.

Table 5
Fitting parameters η and κ for the load ratio F/F_0 in the hardening regime for each specimen in the smooth mineral coated (S-MCF) group, exposed at ambient temperature (20 °C) and at 100 °C.

S-MCF	20 °C						100 °C					
	sp1	sp2	sp3	sp4	sp5	Mean	sp1	sp2	sp3	(sp4)	(sp5)	Mean[a]
η	1.31	1.34	1.54	1.33	1.36	**1.38**	1.14	1.37	1.31	52.56	23.15	**1.27**
std.err.	0.32	0.21	0.28	0.43	0.38	CoV 7%	0.36	0.36	0.10	177.75	6.70	CoV 9%
κ	3.07	3.41	5.41	3.31	3.68	**3.77**	1.42	3.70	3.07	18.96	11.33	**2.74**
std.err.	0.84	0.58	0.98	1.15	1.06	CoV 25%	0.77	1.02	0.26	52.60	2.50	CoV 43%

[a] Excluding sp4 and sp5.

Table 6
Fitting parameters η and κ for the load ratio F/F_0 in the hardening regime, for each specimen in the mineral coated winded group (W-MCF), exposed at ambient temperature (20 °C) and at 100 °C.

W-MCF	20 °C						100 °C					
	sp1	sp2	sp3	sp4	(sp5)	Mean[a]	sp1	(sp2)	(sp3)	sp4	sp5	Mean[b]
η	1.27	1.38	1.18	1.22	7.57	**1.26**	1.12	12.32	32.43	3.58	1.14	**1.95**
std.err.	0.04	0.34	0.07	0.18	1.02	CoV 6%	0.60	3.51	9.72	0.27	0.09	CoV 73%
κ	2.74	3.77	1.81	2.26	10.84	**2.67**	1.28	10.39	9.30	3.23	1.39	**1.97**
std.err.	0.10	0.98	0.16	0.42	1.25	CoV 32%	1.23	2.36	1.83	0.18	0.20	CoV 55%

[a] Excluding sp5.
[b] Excluding sp2 and sp3.

Interestingly, S-MCF exhibits the highest toughness A_1, while the CoV remains limited across all groups. This can be explained by the fact that S-MCF also features superior bond quality, in the form of a slightly larger η, this observation supporting the idea that the interface with the matrix is stronger. Indeed, this result is also accompanied by a significantly higher value of κ, which suggests that this effective bond with the matrix translates into a shorter transfer length required to transmit the applied axial force F to the surrounding matrix [73]. Nonetheless, fitting ambient temperature data produces comparable values for the coefficients of variation (CoV) of all mechanical parameters under consideration, which fact supports the idea that the analysis is meaningful of the underlying mechanical response and that, in fact, all test groups perform similarly at ambient temperature (20 °C), regardless of the type of impregnation.

When observing results concerning the specimens exposed at 100 °C, an important drop of all mechanical properties can be consistently

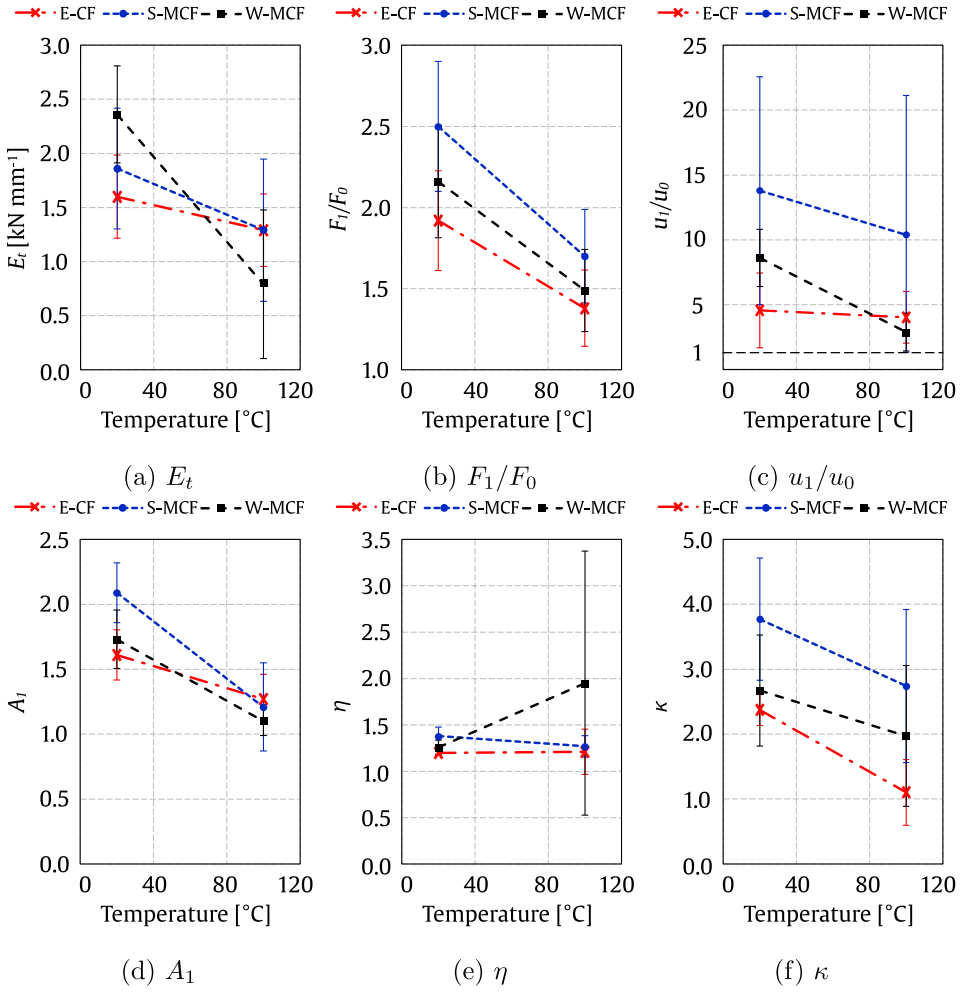

Fig. 13. Mechanical parameters: comparison between epoxy coated (ECF), smooth (S-MCF) and winded (W-MCF) mineral impregnated fibres as a function of temperature up to 100 °C.

observed, which, unexpectedly, is not especially pronounced for epoxy (ECF). As a notable exception, η for W-MCF shows some improvement, although such gain is associated with a very large CoV, that casts some doubts on its statistical significance. Similar to what is observed at 20 °C, parameters appear to be homogeneous across different groups and trends are consistent, which supports the idea that the analysis is meaningful. Interestingly, S-MCF remains best performing also at 100 °C under all parameters (inasmuch as the unreliable value of η for W-MCF is disregarded), especially in terms of peak deformation u_1. Indeed, although the ratio u_1/u_0 between the peak load elongation and the elongation at the end of the linear regime decreases, S-MCF is the only group for which an increase is observed for the absolute elongation u_1, when comparing performance at 100 °C to that at 20 °C, while suffering similar losses in terms of E_t and F_1 to all other groups. Combined with the highest F_1/F_0 ratio among all groups at 100 °C, the post-elastic performance of S-MCF far exceeds that of the other technologies, and especially with respect to ECF. Indeed, ECF suffers major losses in terms of κ and peak force F_1, which suggests more pronounced degradation under exposure. Finally, a dramatic drop in stiffness is recorded for W-MCF, which falls from the highest value of E_t at ambient temperature (20 °C) to the poorest at 100 °C, with ECF and S-MCF being 63 % stiffer. This seems to demonstrate that the surface profiling obtained by winding is particularly delicate and greatly suffers from temperature degradation. This phenomenon is entirely due to the manufacturing process of the impregnated roving, since the matrix and fibre composition are the same of S-MCF, which appears to be the least vulnerable to temperature. In fact, the shrinkage of the AAC matrix due to thermal exposure may lead to radial cracks in the vicinity of the W-MCF ribs, that result in a remarkable stiffness loss, as envisaged in Section 3. This outcome is particularly interesting and deserves further investigation, as there appear very few contributions in the literature that point to the influence of the roving manufacturing process on its temperature vulnerability. In fact, the vast majority of studies tend to focus on the impregnation matrix. Overall, epoxy impregnation, up to 100 °C, is less temperature sensitive than might be expected, although this result may be explained by the shielding effect offered by the large matrix block used in the tests and by the fairly limited temperature being considered. In fact, raising the temperature to 200 °C results in dramatic performance losses across all groups and especially for ECF specimens, to the point that the mechanical model is no longer able to provide a meaningful analysis.

5. Concluding remarks

On the wake of the growing demand for sustainable solutions for the construction industry, mineral impregnated carbon fibres (MCFs) stand out as an advanced reinforcement technology with interesting advantages over traditional steel reinforcement or FRP systems. This paper investigates the interfacial bond of MCF embedded in alkali-activated concrete (AAC), with special regard to the effect of temperature exposure and surface profiling. The custom-made AAC matrix offers an interesting balance of thermal resistance and mechanical performance, while presenting good workability as well as mild environmental impact. Mineral impregnation, based on geopolymers (GPs) and manufactured in an automated continuous pultrusion process, undergoes a

distinctive post-treatment for fast-setting and surface profiling, which is also highly scalable for efficient industrial manufacturing. The investigation shows that, at room temperature, MCF bond performance is comparable to that of commercially available epoxy-impregnated CF rovings. In contrast, MCF demonstrates superior performance at elevated temperature and, in fact, over 50 % of the ambient temperature bond strength is retained up to 200 °C for both MCF types. Indeed, thermal resistance of the MCF is primarily connected with the stability of the mineral impregnation agent and, to some extent, with the capability of the AAC matrix to resist thermal strains, as it is confirmed under various analyses including TGA, dilatometry, ESEM, MIP and μCT. Also, smooth and wound MCFs exhibit distinct pull-out curves which highlight the role of chemical and physical features on the bonding strength. Indeed, epoxy-impregnated rovings mostly rely on a physical interlocking mechanism, in the absence of strong chemical compatibility with the matrix, and therefore frictional resistance dominates the post-cracking response. In contrast, GP impregnation enhances chemical bonding with the matrix, that improves the peak cracking strength. Besides, the adoption of custom-made surface profiling is also investigated and it is shown to greatly enhance the composite stiffness at room temperature, although the benefit is mostly lost after temperature exposure. This outcome is determined by the fact that surface grooves are weakened by temperature and so is the surrounding concrete with which they interact. An analytical one-dimensional stress-and-friction-based mechanical model is employed to interpret experimental data and quantitatively assess some indices characterising the bond quality of the considered technologies. The model presented supports optimal chemical affinity at room temperature and offers the best temperature resistance through the adoption of geopolymer impregnation technology, without the use of additional surface profiling on the roving structure. Although very promising, the results here reported provide only the first tentative approach to highlight the potential of MCF systems and further research is needed to gain a comprehensive understanding of the phenomena associated with mineral impregnation in brittle composites.

Funding

This research is also funded by the European Social Fund and co-financed by tax funds based on the budget approved by the members of the Saxon State Parliament under project LIP/KAKO 2019_TUD (No. 100380876). The financial support of the German Research Foundation (Deutsche Forschungsgemeinschaft, DFG) in the framework of the Research Training Group (Graduiertenkollegs, GRK) 2250, entitled "*Mineral-bonded composites for enhanced structural impact safety*" (grant nr. 287321140) is also gratefully acknowledged. ML acknowledges financial support under the long-term visiting program by the University of Modena and Reggio Emilia. AN and CS are also grateful to the Italian National Group of Mathematical Physics (GNFM), and specifically CS was supported by the Young Researcher scheme 2020 (Approved by Prot. U-UFMBAZ-2021-000072). AN gratefully acknowledges support from the Next Generation EU PRIN 2022 research project "Sustainable CompositE materials for the construction iNdusTry (SCENT)" (grant nr. P2022P3Y2T).

CRediT authorship contribution statement

Jitong Zhao: Writing – review & editing, Writing – original draft, Visualization, Validation, Methodology, Investigation, Formal analysis, Data curation, Conceptualization. **Cesare Signorini:** Writing – review & editing, Writing – original draft, Visualization, Validation, Project administration, Methodology, Investigation, Formal analysis, Data curation, Conceptualization. **Andrea Nobili:** Writing – review & editing, Writing – original draft, Visualization, Validation, Resources, Methodology, Investigation, Funding acquisition, Formal analysis, Data curation, Conceptualization. **Marco Liebscher:** Writing – review & editing, Supervision, Project administration, Funding acquisition, Conceptualization. **Jan Kohout:** Writing – review & editing, Investigation. **Pavlína Hájková:** Investigation. **Viktor Mechtcherine:** Writing – review & editing, Supervision, Resources.

Declaration of competing interest

The authors declare that they have no known competing financial interests or personal relationships that could have appeared to influence the work reported in this paper.

Data availability

Data will be made available on request.

Appendix A. List of symbols

l_0	length of the roving emerging from the matrix
t	roving embedding (anchoring) length in the matrix
$0 < x < t$	axial coordinate alongside the roving inside the matrix
$0 < s < t$	crack length, i.e. $x < s$ is the crack zone, where $\tau = \tau_s$, $s < x < t$ is the uncracked zone where τ is given by (1)
$\zeta = x/t$	dimensionless axial coordinate normalised to the embedding length
F_0, u_0	force and displacement in the pull-out test at the limit of the linear regime
E_t	roving stiffness in the linear regime, related to Young's modulus of the roving
F_1, u_1	peak force and corresponding displacement in the pull-out test
τ_m	maximum shear stress which is supported by the undamaged matrix
τ_s	shear stress supported by the damaged (cracked) matrix
$\eta = \tau_m/\tau_s$	> 1, ratio of the maximum stresses in the undamaged and damaged matrix (friction)
$\chi = \kappa t^{-1}$	exponential decay rate for the stress in the undamaged matrix, closely related to the extinction length L_e
A_1	(dimensionless) area under the F/F_0 vs. ζ curve in the hardening regime (ratio of the hardening toughness over the stored elastic energy)

Appendix B. Residuals

Fig. B.14 shows the hardening curve for specimen 5 in the EP 20 °C group, alongside the nonlinear model (3), whose parameters η and κ have been obtained by best fitting. The other sample groups recorded similar residual ranges, in any cases lower than 10%.

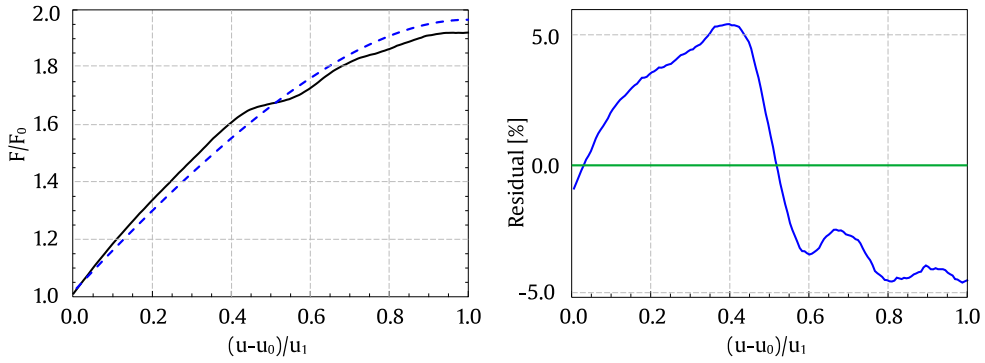

Fig. B.14. F/F_0 dataset (solid, black) for specimen 5 in the EP 20 °C group superposed onto the nonlinear fit (3) (dashed, green). On the right panel, the interpolation residual (i.e. the difference between the actual and the interpolated values) is plotted as a function of the dimensionless elongation, from u_0 to u_1. (For interpretation of the references to colour in this figure legend, the reader is referred to the web version of this article.)

References

[1] D. Dvorkin, A. Poursaee, A. Peled, W.J. Weiss, Influence of bundle coating on the tensile behavior, bonding, cracking and fluid transport of fabric cement-based composites, Cem. Concr. Compos. 42 (2013) 9–19, http://dx.doi.org/10.1016/j.cemconcomp.2013.05.005.

[2] T. Liu, X. Liu, P. Feng, A comprehensive review on mechanical properties of pultruded FRP composites subjected to long-term environmental effects, Composites B 191 (2020) 107958, http://dx.doi.org/10.1016/j.compositesb.2020.107958.

[3] B. Banholzer, T. Brockmann, W. Brameshuber, Material and bonding characteristics for dimensioning and modelling of textile reinforced concrete (TRC) elements, Mater. Struct. 39 (2006) 749–763, http://dx.doi.org/10.1617/s11527-006-9140-x.

[4] Z. Cohen, A. Peled, Effect of nanofillers and production methods to control the interfacial characteristics of glass bundles in textile fabric cement-based composites, Composites A 43 (6) (2012) 962–972, http://dx.doi.org/10.1016/j.compositesa.2012.01.022.

[5] C. Signorini, A. Sola, A. Nobili, Hierarchical composite coating for enhancing the tensile behaviour of textile-reinforced mortar (TRM), Cem. Concr. Compos. 140 (2023) 105082, http://dx.doi.org/10.1016/j.cemconcomp.2023.105082.

[6] R.-M. María, V.-L. Paula, F.-G. Jaime, L.-R. Jorge, Improvement of tensile properties of carbon fibre-reinforced cementitious matrix composites with coated textile and enhanced mortars, Constr. Build. Mater. 369 (2023) 130552, http://dx.doi.org/10.1016/j.conbuildmat.2023.130552.

[7] A. Asgharzadeh, M. Raupach, Durability behavior of polymer impregnated carbon textiles in alkaline solution as CP anode, Mater. Corros. 70 (2) (2019) 345–356, http://dx.doi.org/10.1002/maco.201810098.

[8] J. Donnini, F.D.C. y Basalo, V. Corinaldesi, G. Lancioni, A. Nanni, Fabric-reinforced cementitious matrix behavior at high-temperature: Experimental and numerical results, Compos. B-Eng 108 (2017) 108–121, http://dx.doi.org/10.1016/j.compositesb.2016.10.004.

[9] M. Messori, A. Nobili, C. Signorini, A. Sola, Mechanical performance of epoxy coated AR-glass fabric textile reinforced mortar: Influence of coating thickness and formulation, Compos. B-Eng 149 (2018) 135–143, http://dx.doi.org/10.1016/j.compositesb.2018.05.023.

[10] T. Gong, A.H. Ahmed, I. Curosu, V. Mechtcherine, Tensile behavior of hybrid fiber reinforced composites made of strain-hardening cement-based composites (SHCC) and carbon textile, Constr. Build. Mater. 262 (2020) 120913, http://dx.doi.org/10.1016/j.conbuildmat.2020.120913.

[11] I. Kruppke, M. Butler, K. Schneider, R.-D. Hund, V. Mechtcherine, C. Cherif, Carbon fibre reinforced concrete: dependency of bond strength on Tg of yarn impregnating polymer, Mater. Sci. Appl. 10 (4) (2019) 328–348, http://dx.doi.org/10.4236/msa.2019.104025.

[12] M. Scheurer, M. Kalthoff, T. Matschei, M. Raupach, T. Gries, Analysis of curing and mechanical performance of pre-impregnated carbon fibers cured within concrete, Textiles 2 (4) (2022) 657–672, http://dx.doi.org/10.3390/textiles2040038.

[13] D. Zhu, X. Bai, Q. Yao, M.Z. Rahman, X. Li, T. Yang, S. Guo, Effects of volume fraction and surface coating of textile yarns on the tensile performance of AR-glass textile reinforced concrete, J. Build. Eng. 71 (2023) 106420, http://dx.doi.org/10.1016/j.jobe.2023.106420.

[14] J.P. Firmo, J.R. Correia, L.A. Bisby, Fire behaviour of FRP-strengthened reinforced concrete structural elements: A state-of-the-art review, Composites B 80 (2015) 198–216, http://dx.doi.org/10.1016/j.compositesb.2015.05.045.

[15] M. Messori, A. Nobili, C. Signorini, A. Sola, Effect of high temperature exposure on epoxy-coated glass textile reinforced mortar (GTRM) composites, Constr. Build Mater. 212 (2019) 765–774, http://dx.doi.org/10.1016/j.conbuildmat.2019.04.026.

[16] V. Bertolli, C. Signorini, A. Nobili, T. D'Antino, Influence of severe thermal preconditioning on the bond between carbon FRCM and masonry substrate: Effect of textile pre-impregnation, Constr. Build. Mater. 409 (2023) 134028, http://dx.doi.org/10.1016/j.conbuildmat.2023.134028.

[17] C. Signorini, A. Nobili, Targeting functionalised carbon nanotubes at the interphase of Textile Reinforced Mortar (TRM) composites, Composites A 144 (2021) 106330, http://dx.doi.org/10.1016/j.compositesa.2021.106330.

[18] C. Signorini, A. Sola, A. Nobili, C. Siligardi, Lime-cement Textile Reinforced Mortar (TRM) with modified interphase, J. Appl. Biomater. Funct. 17 (1) (2019) 2280800019827823, http://dx.doi.org/10.1177/2280800019827823.

[19] K. Schneider, M. Lieboldt, M. Liebscher, M. Fröhlich, S. Hempel, M. Butler, C. Schröfl, V. Mechtcherine, Mineral-based coating of plasma-treated carbon fibre rovings for carbon concrete composites with enhanced mechanical performance, Materials 10 (4) (2017) 360, http://dx.doi.org/10.3390/ma10040360.

[20] C. Signorini, A. Nobili, M. Liebscher, J. Zhao, A.H. Ahmed, T. Köberle, V. Mechtcherine, Assessing the stress-transfer capability of mineral impregnated PBO yarns in a limestone calcined clay cement-based (LC^3) matrix, Composites B 276 (2024) 111364, http://dx.doi.org/10.1016/j.compositesb.2024.111364.

[21] V. Mechtcherine, A. Michel, M. Liebscher, K. Schneider, C. Großmann, Mineral-impregnated carbon fiber composites as novel reinforcement for concrete construction: Material and automation perspectives, Autom. Constr. 110 (2020) 103002, http://dx.doi.org/10.1016/j.autcon.2019.103002.

[22] J. Zhao, M. Liebscher, A. Michel, K. Schneider, R. Foest, M. Fröhlich, A. Quade, V. Mechtcherine, Plasma-generated silicon oxide coatings of carbon fibres for improved bonding to mineral-based impregnation materials and concrete matrices, Cem. Concr. Compos. 114 (2020) 103667, http://dx.doi.org/10.1016/j.cemconcomp.2020.103667.

[23] J. Zhao, M. Liebscher, K. Schneider, D. Junger, V. Mechtcherine, Effect of surface profiling on the mechanical properties and bond behaviour of mineral-impregnated, carbon-fibre (MCF) reinforcement based on geopolymer, Constr. Build. Mater. 367 (2023) 130199, http://dx.doi.org/10.1016/j.conbuildmat.2022.130199.

[24] T. Neef, S. Müller, V. Mechtcherine, 3D-druck mit carbonbeton: Technologie und die ersten untersuchungsergebnisse, Beton- und Stahlbetonbau 115 (2020) 943–951, http://dx.doi.org/10.1002/BEST.202000069.

[25] J. Zhao, M. Liebscher, T. Köberle, A. Almanla, V. Mechtcherine, Mineral-impregnated carbon-fiber (MCF) composites made with differently sized fly-ash geopolymers for durable light weight and high temperature applications, Cem. Concr. Compos. (2023) 104950, http://dx.doi.org/10.1016/J.CEMCONCOMP.2023.104950.

[26] J. Zhao, M. Liebscher, A. Michel, D. Junger, A.C.C. Trindade, F. de Andrade Silva, V. Mechtcherine, Development and testing of fast curing, mineral-impregnated carbon fiber (MCF) reinforcements based on metakaolin-made geopolymers, Cem. Concr. Compos. 116 (2021) 103898, http://dx.doi.org/10.1016/j.cemconcomp.2020.103898.

[27] D. Junger, M. Liebscher, J. Zhao, V. Mechtcherine, Joule heating as a smart approach in enhancing early strength development of mineral-impregnated carbon-fibre composites (MCF) made with geopolymer, Composites A 153 (2022) 106750, http://dx.doi.org/10.1016/J.COMPOSITESA.2021.106750.

[28] P. He, D. Jia, T. Lin, M. Wang, Y. Zhou, Effects of high-temperature heat treatment on the mechanical properties of unidirectional carbon fiber reinforced geopolymer composites, Ceram. Int. 36 (2010) 1447–1453, http://dx.doi.org/10.1016/j.ceramint.2010.02.012.

[29] M. Welter, Unidirectional Fibre Reinforced Geopolymer Matrix Composites (Ph.D. thesis), Victoria University of Wellington, 2013.

[30] T. Doan, P. Louda, D. Kroisova, O. Bortnovsky, N. Thang, New generation of geopolymer composite for fire-resistance, Adv. Compos. Mater. - Anal. Nat. Man-Made Mater. (2011) http://dx.doi.org/10.5772/17933.

[31] J. Zhao, A.C.C. Trindade, M. Liebscher, F.d. Silva, V. Mechtcherine, A review of the role of elevated temperatures on the mechanical properties of Fiber-Reinforced Geopolymer (FRG) composites, Cem. Concr. Compos. 137 (2023) 104885, http://dx.doi.org/10.1016/J.CEMCONCOMP.2022.104885.
[32] D. Ribero, W.M. Kriven, Properties of geopolymer composites reinforced with basalt chopped strand mat or woven fabric, J. Am. Ceram. Soc. 99 (2016) 1192–1199, http://dx.doi.org/10.1111/jace.14079.
[33] E. Haincová, P. Hájková, J. Kohout, Prepregs for temperature resistant composites, Materials 12 (2019) http://dx.doi.org/10.3390/ma12234012.
[34] F. Bencardino, A. Condello, Eco-friendly external strengthening system for existing reinforced concrete beams, Composites B 93 (2016) 163–173, http://dx.doi.org/10.1016/j.compositesb.2016.03.022.
[35] K. Heng, N. Areemit, P. Chindaprasirt, Behavior of concrete cylinders confined by a ferro-geopolymer jacket in axial compression, Eng. Appl. Sci. Res. 44 (2) (2017) 90–96.
[36] X. Shen, W. Chen, B. Li, C.M. Hancock, Y. Xu, Flexural strengthening of reinforced concrete beams using fabric reinforced alkali-activated slag matrix, J. Build. Eng. 33 (2021) 101865, http://dx.doi.org/10.1016/j.jobe.2020.101865.
[37] S. Cholostiakow, L.N. Koutas, C.G. Papakonstantinou, Geopolymer versus cement-based textile-reinforced mortar: Diagonal compression tests on masonry walls representative of infills in RC frames, Constr. Build. Mater. 373 (2023) 130836, http://dx.doi.org/10.1016/j.conbuildmat.2023.130836.
[38] H.-y. Zhang, X. Hao, W. Fan, Experimental study on high temperature properties of carbon fiber sheets strengthened concrete cylinders using geopolymer as adhesive, Procedia Eng. 135 (2016) 47–55, http://dx.doi.org/10.1016/j.proeng.2016.01.078.
[39] H.Y. Zhang, H.R. Lv, V. Kodur, S.L. Qi, Performance comparison of fiber sheet strengthened RC beams bonded with geopolymer and epoxy resin under ambient and fire conditions, J. Struct. Fire Eng. 9 (3) (2018) 174–188, http://dx.doi.org/10.1108/JSFE-01-2017-0023.
[40] A. Kelly, Interface effects and the work of fracture of a fibrous composite, Proc. R. Soc. Lond. Ser. A Math. Phys. Eng. Sci. 319 (1970) 95–116, http://dx.doi.org/10.1098/rspa.1970.0168.
[41] J.W. Hutchinson, H.M. Jensen, Models of fiber debonding and pullout in brittle composites with friction, Mech. Mater. 9 (1990) 139–163, http://dx.doi.org/10.1016/0167-6636(90)90037-G.
[42] A.E. Naaman, G.G. Namur, J.M. Alwan, H.S. Najm, Fiber pullout and bond slip. I: Analytical study, J. Struct. Eng. 117 (9) (1991) 2769–2790.
[43] E. Radi, L. Lanzoni, A. Sorzia, Analytical modelling of the pullout behavior of synthetic fibres treated with nano-silica, Procedia Eng. 109 (2015) 525–532, http://dx.doi.org/10.1016/j.proeng.2015.06.260.
[44] A. Sorzia, C. Signorini, V. Volpini, P. Di Maida, Analytical approach for modelling the pull-out mechanism of recycled synthetic fibres in fibre-reinforced concrete (FRC), Key Eng. Mater. 919 (2022) 35–46, http://dx.doi.org/10.4028/p-4k539k.
[45] R.J. Kerans, T.A. Parthasarathy, Theoretical analysis of the fiber pullout and pushout tests, J. Am. Ceram. Soc. 74 (1991) 1585–1596, http://dx.doi.org/10.1111/j.1151-2916.1991.tb07144.x.
[46] C. DiFrancia, T.C. Ward, R.O. Claus, The single-fibre pull-out test. 1: Review and interpretation, Composites A 27 (8) (1996) 597–612, http://dx.doi.org/10.1016/1359-835X(95)00069-E.
[47] C. Morales-Cruz, Crack-Distributing Carbon Textile Reinforced Concrete Protection Layers (Ph.D. thesis), Rheinisch-Westfälische Technische Hochschule Aachen, 2020.
[48] SIGRAFIL, Continuous carbon fiber tows, 2022, URL: https://www.sglcarbon.com/en/markets-solutions/material/sigrafil-continuous-carbon-fiber-tows/.
[49] J. Zhao, M. Liebscher, L. Tzounis, V. Mechtcherine, Role of sizing agent on the microstructure morphology and mechanical properties of mineral-impregnated carbon-fiber (MCF) reinforcement made with geopolymers, Appl. Surf. Sci. 567 (2021) 150740, http://dx.doi.org/10.1016/j.apsusc.2021.150740.
[50] M. Liebscher, J. Zhao, G. Wilms, A. Michel, K. Wilhelm, V. Mechtcherine, Influence of roller configuration on the fiber–matrix distribution and mechanical properties of continuously produced, Mineral-Impregnated Carbon Fibers (MCFs), Fibers 10 (5) (2022) 42, http://dx.doi.org/10.3390/fib10050042.
[51] J. Zhao, D. Zhao, M. Liebscher, B. Yin, M. Mohammadi, M. Butler, T. Köberle, M. Kaliske, V. Mechtcherine, Temperature-dependent pullout behavior of geopolymer concrete reinforced with polymer- or mineral-impregnated carbon fiber composites: An experimental and numerical study, ACS Sustain. Chem. Eng. (2023) http://dx.doi.org/10.1021/ACSSUSCHEMENG.3C00592.
[52] UNI EN 196-1, Methods of Testing Cement - Part 1: Determination of Strength, Standard, European Committee for Standardization, 2016.
[53] DIN EN 12390-13:2021-09 1.9.2021 | technical standard | MyStandards, 2021, URL: https://www.mystandards.biz/standard/dinen-12390-13-1.9.2021.html.
[54] Din EN 1015-3 : methods of test for mortar for masonry - part 3: determination of consistence of fresh mortar (by flow table), 2007, URL: https://global.ihs.com/doc_detail.cfm?document_name=DIN%20EN%201015%2D3&item_s_key=00331198.
[55] K. Schneider, A. Michel, M. Liebscher, L. Terreri, S. Hempel, V. Mechtcherine, Mineral-impregnated carbon fibre reinforcement for high temperature resistance of thin-walled concrete structures, Cem. Concr. Compos. 97 (2019) 68–77, http://dx.doi.org/10.1016/j.cemconcomp.2018.12.006.
[56] J. Zhao, A.H. Ahmed, M. Liebscher, A. Bartsch, E. Ivaniuk, M. Butler, J. Kohout, P. Hájková, V. Mechtcherine, Thermomechanical behavior of textile-reinforced geopolymer concrete based on mineral-impregnated carbon-fibers (mcfs) composites, Cement and Concrete Composites (2024) 105555, http://dx.doi.org/10.1016/j.cemconcomp.2024.105555.
[57] R.M. de Castro Silva, J. Zhao, M. Liebscher, I. Curosu, F. de Andrade Silva, V. Mechtcherine, Bond behavior of polymer-and mineral-impregnated carbon fiber yarns towards concrete matrices at elevated temperature levels, Cem. Concr. Compos. 133 (2022) 104685, http://dx.doi.org/10.1016/j.cemconcomp.2022.104685.
[58] S. Sasui, G. Kim, J. Nam, A. van Riessen, M. Hadzima-Nyarko, G. Choe, D. Suh, W. Jinwuth, Effects of waste glass sand on the thermal behavior and strength of fly ash and GGBS based alkali activated mortar exposed to elevated temperature, Constr. Build. Mater. 316 (2022) 125864, http://dx.doi.org/10.1016/j.conbuildmat.2021.125864.
[59] P. Duxson, G.C. Lukey, J.S. van Deventer, Thermal evolution of metakaolin geopolymers: Part 1 – physical evolution, J. Non-Cryst. Solids 352 (2006) 5541–5555, http://dx.doi.org/10.1016/J.JNONCRYSOL.2006.09.019.
[60] D.L.Y. Kong, J.G. Sanjayan, K. Sagoe-Crentsil, Factors affecting the performance of metakaolin geopolymers exposed to elevated temperatures, J. Mater. Sci. 2007 43:3 43 (2007) 824–831, http://dx.doi.org/10.1007/S10853-007-2205-6, URL: https://link.springer.com/article/10.1007/s10853-007-2205-6.
[61] A.C.C. Trindade, M. Liebscher, I. Curosu, F. de Andrade Silva, V. Mechtcherine, Influence of elevated temperatures on the residual and quasi in-situ flexural strength of strain-hardening geopolymer composites (SHGC) reinforced with PVA and PE fibers, Constr. Build. Mater. 314 (2022) 125649, http://dx.doi.org/10.1016/j.conbuildmat.2021.125649.
[62] D.-W. Zhang, X.-M. Sun, Y.-R. Wang, H. Li, Relationship between fractal characteristics of pore-structure and thermal properties of FA-based AAM under different curing conditions, J. Mater. Res. Technol. 26 (2023) 961–972, http://dx.doi.org/10.1016/j.jmrt.2023.07.245.
[63] M.B.M. Salahuddin, M. Norkhairunnisa, F. Mustapha, A review on thermophysical evaluation of alkali-activated geopolymers, Ceram. Int. 41 (2015) 4273–4281, http://dx.doi.org/10.1016/J.CERAMINT.2014.11.119.
[64] H.T. Türker, M. Balçikanli, İ.H. Durmuş, E. Özbay, M. Erdemir, Microstructural alteration of alkali activated slag mortars depend on exposed high temperature level, Constr. Build. Mater. 104 (2016) 169–180, http://dx.doi.org/10.1016/j.conbuildmat.2015.12.070.
[65] E. Lorenz, E. Schütze, F. Schladitz, M. Curbach, Textilbeton - Grundlegende Untersuchungen im Überblick, Beton- und Stahlbetonbau 108 (2013) http://dx.doi.org/10.1002/best.201300041.
[66] R. Füllsack-Köditz, Verbundverhalten von GFK-Bewehrungsstäben und Rissentwicklung in GFK-stabbewehrten Betonbauteilen (Ph.D. thesis), in: Schriftenreihe des Instituts für Konstruktiven Ingenieurbau, 1, 2004, http://dx.doi.org/10.25643/bauhaus-universitaet.227.
[67] F. Micelli, A. Nanni, Durability of FRP rods for concrete structures, Constr. Build. Mater. 18 (2004) 491–503, http://dx.doi.org/10.1016/j.conbuildmat.2004.04.012.
[68] A. Younes, A. Seidel, T. Engler, C. Cherif, D. Ehlig, Mechanical behaviour of carbon and glass filament yarns under high temperatures for composite applications, J. Text. Inst. (2013) http://dx.doi.org/10.1080/00405000.2012.717752.
[69] P. Colombi, T. D'Antino, Analytical assessment of the stress-transfer mechanism in FRCM composites, Compos. Struct. 220 (2019) 961–970, http://dx.doi.org/10.1016/j.compstruct.2019.03.074.
[70] V. Bertolli, T. D'Antino, Modeling the behavior of externally bonded reinforcement using a rigid-trilinear cohesive material law, Int. J. Solids Struct. 248 (2022) 111641, http://dx.doi.org/10.1016/j.ijsolstr.2022.111641.
[71] T. D'Antino, C. Carloni, L.H. Sneed, C. Pellegrino, Matrix–fiber bond behavior in PBO FRCM composites: A fracture mechanics approach, Eng. Fract. Mech. 117 (2014) 94–111, http://dx.doi.org/10.1016/j.engfracmech.2014.01.011.
[72] T. D'Antino, C. Poggi, Characterization and design of multilayer PBO FRCM composite reinforcements for concrete structures, J. Compos. Construct. 25 (6) (2021) 04021048, http://dx.doi.org/10.1061/(ASCE)CC.1943-5614.000115.
[73] L. Bizindavyi, K. Neale, Transfer lengths and bond strengths for composites bonded to concrete, J. Compos. Construct. 3 (4) (1999) 153–160, http://dx.doi.org/10.1061/(ASCE)1090-0268(1999)3:4(153).